RSC Advances

PAPER

View Article Online
View Journal | View Issue

Cite this: *RSC Adv.*, 2016, **6**, 94128

Ionic liquid-enhanced soft resistive switching devices†

Krishna Rajan,[ab] Annalisa Chiappone,[a] Denis Perrone,[a] Sergio Bocchini,[a] Ignazio Roppolo,[a] Katarzyna Bejtka,[a] Micaela Castellino,[a] Candido Fabrizio Pirri,[ab] Carlo Ricciardi[b] and Alessandro Chiolerio*[a]

Received 22nd July 2016
Accepted 27th September 2016

DOI: 10.1039/c6ra18668h

www.rsc.org/advances

Resistive switching phenomena are of paramount importance in the area of memory devices. In the present study, we have fabricated a simple resistive switching device using a solution processable nanocomposite based on silver nitrate and poly(vinylidene fluoride-hexafluoropropylene). The change in resistance is ascribed to an initial ionic conduction, followed by a non-continuous field induced filament formation. The switching device fabricated with the above-mentioned active matrix displayed a volatile switching behavior. The addition of room temperature ionic liquid plays a fundamental role in triggering permanent memory and reducing the set voltage range up to ten-fold. The change in switching behavior with respect to the applied voltage bias and compliance level set during electrical characterization was studied thoroughly. The present work also gives a glimpse into the importance of device architecture on resistive switching phenomena.

1. Introduction

Nowadays, Resistive Switching Devices (RSDs) are gaining significance mainly for their prospective application in the field of digital memories.[1–4] RSD is a brand new technological device, which can vertically change the concept of computing architecture. It can be used to perform analog computing at digital speeds, which could be a fundamental turning point in the field of electronics. It was in 1971 when Chua mathematically came up with the missing memristor.[5] At that time it was considered a mere mathematical model, until HP disclosed the first example of a physical memristor in 2008.[6] A Pt/TiO_2/Pt structure was claimed to be completely in agreement with Chua's memristor model. Since then, this topic has been intensively studied and a lot of similar[7–9] and contradictory results[10] were presented. RSDs are classified into organic, inorganic and hybrid, according to the nature of the active layer that is present between the two electrodes or leads. Inorganic RSDs represent the most widely studied case due to their simpler switching matrix compared to organic and hybrid RSDs.[11] Thin film based RSDs are good examples of inorganic RSDs, where a careful control of the active material thickness allows to electrically tune certain properties and to modulate the current flowing perpendicularly to the same film.[12,13] Nanocomposite (NC) RSDs, alternatively known as hybrid, feature a matrix and an active filler that do not share the same electronic behavior. NC RSDs are normally characterized by a passive matrix containing dispersion of active fillers in the form of clusters or nanoparticles (NPs), which can be electrically activated and can also produce current modulation.[14,15] Extensive research and studies were conducted on RSDs based on different switching matrices,[16–18] each of which has its unique properties. Organic RSDs exploit the intrinsic properties of organic materials, including processability, low cost, good retention time, high endurance and mechanical flexibility, when coupled with polymeric or natural flexible substrates.

In RSDs, the Resistive Switching (RS) effect in most cases is caused by the formation of conducting filaments;[19–24] in particular, electrochemical metallization (ECM) memories feature a filament composed of reduced metal (produced by migration of the metallic electrodes) through the polymeric matrix. ECM memories can be regarded as the next generation memory devices, due to the possibility of scaling down almost to the atomic level, while taking advantage of a fast read/write/erase process and a long retention period.[25,26] Usually, the layout of RSDs consists of a stacked structure in which the intermediate layer is composed of a very thin film (≈100 nm or less) of polymeric material. Active electrodes or polymers containing metal ions that can be reduced by an applied voltage are used in order to create the conductive filament across the polymer. The presence of polar atoms (*e.g.* oxygen or fluorine) in the polymeric chain that can coordinate metal ions, regardless of their position (side or principal chain), is essential for the production of metal filaments.[27] Adding an ionic liquid (IL) increases ionic

[a]*Center for Space Human Robotics, Istituto Italiano di Tecnologia, Corso Trento 21, 10129, Torino, Italy. E-mail: alessandro.chiolerio@iit.it*

[b]*Department of Applied Science and Technology, Politecnico Di Torino, C. so Duca degli Abruzzi 24, 10129 Torino, Italy*

† Electronic supplementary information (ESI) available. See DOI: 10.1039/c6ra18668h

conductivity by enhancing the metal ions mobility, which finally decreases the voltage necessary for the device switching. These IL incorporated RSDs fall under the category of redox-based RS memories. In such cases, RS takes place by the dissolution of a conducting filament in a metal/ionic conductor/metal structure under the influence of an electric field. Krishnan *et al.* explained the mechanism of RS by giving direct evidence of the metallic conductive filament formation, occurring between the electrodes as a result of an applied electric field.[28] A great deal of research was carried out to clarify the effects of ILs in enhancing the ionic transport in crystalline polymer matrices.[29–31] Such compounds are normally used as non-volatile liquid electrolytes (IL with low vapour pressure) in electrochemical applications, as they assure a wide electrochemical stability window and high ionic conductivity, which are considered as key factors for a good electrolyte.[32,33] In the present work, poly vinylidene fluoride-hexafluoropropylene (PVDF-HFP) was used as the polymer matrix due to its high dielectric constant, good mechanical strength and also due to its chemical stability.[34,35] The presence of HFP in PVDF reduces its crystallinity, thus making it soluble in a wide range of solvents. The PVDF-HFP matrix acts as a quasi-solid medium for the silver ions, supporting their movements when an electric field is applied. Furthermore, it was also observed that the addition of a room temperature IL 1-butyl-3-methyl imidazolium bis(trifluoro methylsulfonyl)imide (BMI-TFSI) to PVDF matrix drastically influenced its electrical characteristics.[36] It is important to underline that the proposed matrix is totally compatible with flexible substrates, a fact that widens its range of applications; in fact, there is a great deal of microelectronic thrust that is focusing on the development of new materials, which can be easily and cost effectively deposited on a variety of substrates like paper, fabrics and plastics,[37] making them an attractive component for printed electronics. Moreover, the formulation is processed at room temperature, which is one of the foremost properties that allows the material to be deposited on the cheapest flexible substrates, including paper. The achievable device uniformity,[38] the cheaper production method and the easy deposition technique along with the advantage of room temperature processing make these NCs very promising in the field of disposable devices.

2. Experimental section

2.1. Materials

Poly(vinylidene fluoride-hexafluoropropylene) (PVDF-HFP) Kynar-Superflex 2500 (pellets) with a 20 wt% of hexafluoropropylene and a density of 1.79 g cm^{-3} was purchased from Arkema, 1-butyl-3-methylimidazolium bis(trifluoromethanesulfonyl)imide (BMIM TFSI) (98%), silver nitrate ($AgNO_3$) (99%), dimethylformamide (99.5%) (DMF) were purchased from Sigma Aldrich.

2.2. Device fabrication

The active switching matrix was prepared as follows: a solution of PVDF-HFP (10 wt%) in DMF was prepared by vigorous stirring for 45 minutes. $AgNO_3$ was then added to the above polymer solution and sonicated for 20 minutes obtaining a clear solution. BMIM-TFSI was added directly to the above solution and sonicated for 20 minutes [Fig. 1(b)]. The solutions were spin coated at room temperature onto the substrates at 3000 rpm for 20 seconds. In the present case, the thickness of the spin coated matrix was found to be around 1 μm. The exact composition of PVDF/$AgNO_3$ (further in the text: PAG) was 95/5 while the sample containing IL (PAG–IL) had a ratio PVDF/$AgNO_3$/IL of 65/5/30.

In order to investigate the effect of the electrodes and the device architecture, two different structures have been studied. In the first case, we adopted a planar design, unlike other cases, where RSDs feature a layered structure.[39–42] This approach was chosen in order to decouple the problem of fabricating controlled electrode gaps and NC deposition through the gap. In planar configuration, the device has identical gold electrodes deposited on substrates obtained from a (100) oriented silicon wafer. The electrodes fabrication process started with the growth of a SiO_2 layer (200 nm thick) on both wafer sides, by using a dry oxidation process in a quartz tube furnace. Then, gold electrodes were deposited using an electron beam evaporator (ULVAC EBX-14D). A Ti layer (10 nm thick) was used in order to promote the adhesion of the Au layer (100 nm thick) to the substrate. Both layers were grown using a deposition rate of 0.3 nm s^{-1}. Electrodes were patterned using AZ5214E photoresist (Microchemicals) in a standard UV photolithographic process with the aid of a Neutronix Quintel NXQ 4006 mask aligner. After photolithography, the Au layer was selectively etched using a solution made by iodine (I_2) and potassium iodide (KI) in water, with an estimated etch rate of 0.2 nm s^{-1}. The underlying Ti layer was etched using a solution of hydrofluoric acid (HF) and hydrogen peroxide (H_2O_2) in water. Finally, the substrates were diced using a diamond dicing saw, in order to obtain samples with an area of 5 mm × 7 mm, each

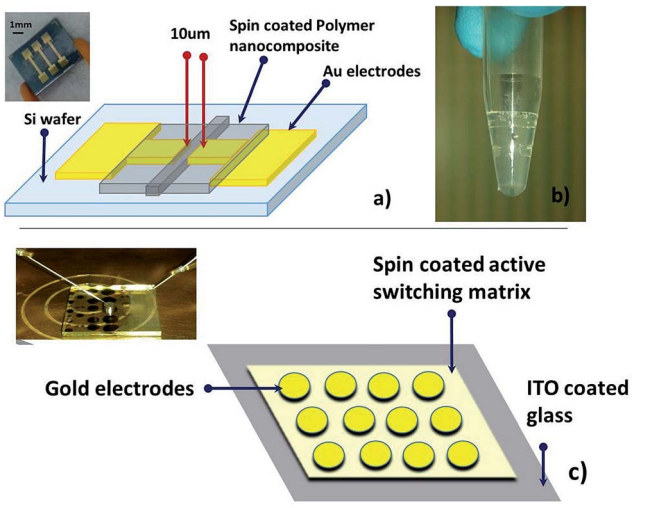

Fig. 1 (a) Schematic representation of the planar device with spin coated polymer NC, inset: physical device after polymer NC deposition. (b) Polymer NC solution before deposition. (c) Schematic representation of the stacked device, inset: physical device under electrical characterization.

with three identical Ti/Au electrodes. The electrodes have a width of 300 μm, and they are separated by a 10 μm gap.

Fig. 1(a) shows the schematic representation of the planar device with symmetrical Au electrodes and the inset shows the final spin coated device. The RS is attributed to the chemical and physical transformation occurring in the 10 μm gap between the Au electrodes. In the second case, we developed a stacked structure, which is the most commonly used RSD design due to its thinner active layer and its enhanced scalability. This structure comprises a glass substrate with an Indium Tin Oxide (ITO) coating as bottom electrode (BE). Once the active NC is spin-coated (≈400 nm) onto the ITO-coated glass substrate, Au electrodes of 100 nm thickness were deposited as top electrodes (TE), using a shadow mask [Fig. 1(c)].

2.3. Materials characterization

FT-IR transmittance spectra were collected on a Tensor 27 FTIR spectrometer (Bruker). The samples were prepared by spin-coating the two formulations on a Si wafer using the same conditions of RSDs. The averaged signal was collected with a resolution of 2 cm^{-1} from 4000 to 600 cm^{-1}.

Field Emission Scanning Electron Microscopy (FESEM, ZEISS Dual Beam Auriga) was used for morphological analysis of nanocomposite on the planar structure.

Differential Scanning Calorimetry (DSC) was carried out on PVDF-HFP, PAG and PAG–IL films. The results were acquired using DSC 204 F1 Phoenix® (Netzsch) instrument under a continuous nitrogen flow of 50 ml per minute. The samples were cooled from room temperature to −50 °C and heated to 250 °C at the rate of 10 °C per minute.

X-ray photoelectron spectroscopy (XPS) studies were carried out by a PHI 5000 Versaprobe scanning X-ray photoelectron spectrometer (monochromatic Al K-alpha X-ray source with 1486.6 eV energy, 15 kV voltage, and 1 mA anode current) in order to investigate surface chemical composition. A spot size of 50 μm was used to collect the photoelectron signal for both the high resolution (HR) and the survey spectra. The X-ray spot was placed between the gold electrodes to collect signals all around the gap. Different pass energy values were employed: 187.85 eV for survey spectra and 23.5 eV for HR peaks. All samples were analyzed using a combined electron and argon ion gun neutralizer system to reduce the charging effect during the measurements. Spectra were analyzed using Multipak 9.6 software. All core-level peak energies were referenced to C1s peak at 284.5 eV (C–C/C–H sp^2 bonds), the background contribution in HR scans has been subtracted by means of a Shirley function and the deconvolution procedure has been done using Gaussian–Lorentzian mixed functions.

Electrical characterizations were performed by using Keithley 4200-SCS semiconductor characterization system. The characterization of the device with a planar configuration was carried out using tungsten (W) micro probes, which were directly placed in contact with the gold electrodes in order to maintain electrical connection. On the other hand, the stacked configuration with asymmetrical electrodes were probed using a cylindrical structure (both diameter and height were 2 mm), which was kept in contact with the gold TE, and then the W needle was kept on the cylinder thus achieving connection with the system (inset Fig. 1(c)). The connection to the ITO BE was made directly through the W needle. In the stacked asymmetrical electrode configuration, the active bias was provided to ITO, while Au electrode was kept as the reference electrode (0 V). The electrical characterization was carried out in air at room temperature.

Viscosity of the polymer–silver nitrate solution was measured using an Anton Paar MCR 302 Modulator Compact Rheometer. The solution exhibited a newtonian fluid characteristic.

3. Results and discussion

3.1. FT-IR analyses

The spectrum of PAG [Fig. 2(a)] is mainly related to PVDF-HFP; the band at 1398 cm^{-1} is composed of CH_2 wagging and CH_2 scissoring vibration of vinylidene; the band at 1313 cm^{-1} is the symmetrical stretching of CF_3; the band at 1177 cm^{-1} corresponds to CF_2 stretching; 1072 cm^{-1} band is the symmetric C–F stretching; the bands at 872 and 850 cm^{-1} are the wagging and rocking of the vinylidene.[43] The peaks at 509–485 cm^{-1} arise due to Ag–O bond,[44] while no signature of residual silver nitrate is observed. It can be supposed that during deposition of $AgNO_3$ the salt once dissolved in the PVDF-HFP tends to degrade to AgO and the corresponding nitrogen oxide/oxides.

In the PAG–IL spectrum [Fig. 2(b)], the main absorbance due to PVDF-HFP are still present: the band at 1406 cm^{-1} corresponds to vinylidene CH_2 wagging and CH_2 scissoring vibration, while the wagging and rocking of the vinylidene bands are still present at 880 and 837 cm^{-1}.[43] The other bands are partially superimposed with the C–F vibrations of IL. The bands 1354 cm^{-1}, 1204 cm^{-1}, and 1060 cm^{-1} are associated with the presence of C–F and SO_2 stretching of bis(trifluoromethanesulfonyl)imide.[45] The absorbance in 2800 to 3200 cm^{-1} region is mainly due to the 1-butyl-3-methyl imidazolium cation (BMIM). The butyl chain attached to the imidazolium ring exhibits peaks at 2968 and 2877 cm^{-1}. The CH_3 symmetric and antisymmetric stretching, and the CH_2 antisymmetric stretching are located at 2938 cm^{-1}.[46,47] Other peaks in the 3050–2800 cm^{-1} region are difficult to recognize unless the 3019 cm^{-1} peak that is arising from the CH_2 antisymmetric stretching of PVDF-HFP.[48] Bands above 3050 cm^{-1} are from the C–H vibrational modes of the imidazolium ring, peaks at 3120 and 3157 cm^{-1} are for antisymmetric and symmetric stretch vibrational modes of HC(4)–C(5)H of BMIM and the peak shown as the shoulder around 3100 cm^{-1} is assigned to the stretch vibrational mode of C(2)–H(3).[49,50] Finally, in the 2000–1500 cm^{-1} region, two peaks are present. The first at 1570 cm^{-1} is due to the C–C stretching of the BMIM ring and the second at 1724 cm^{-1} is probably due to the presence of DMF solvent residues that are difficult to eliminate being miscible with the IL.[51] In this case, no bands corresponding to silver oxide were present.

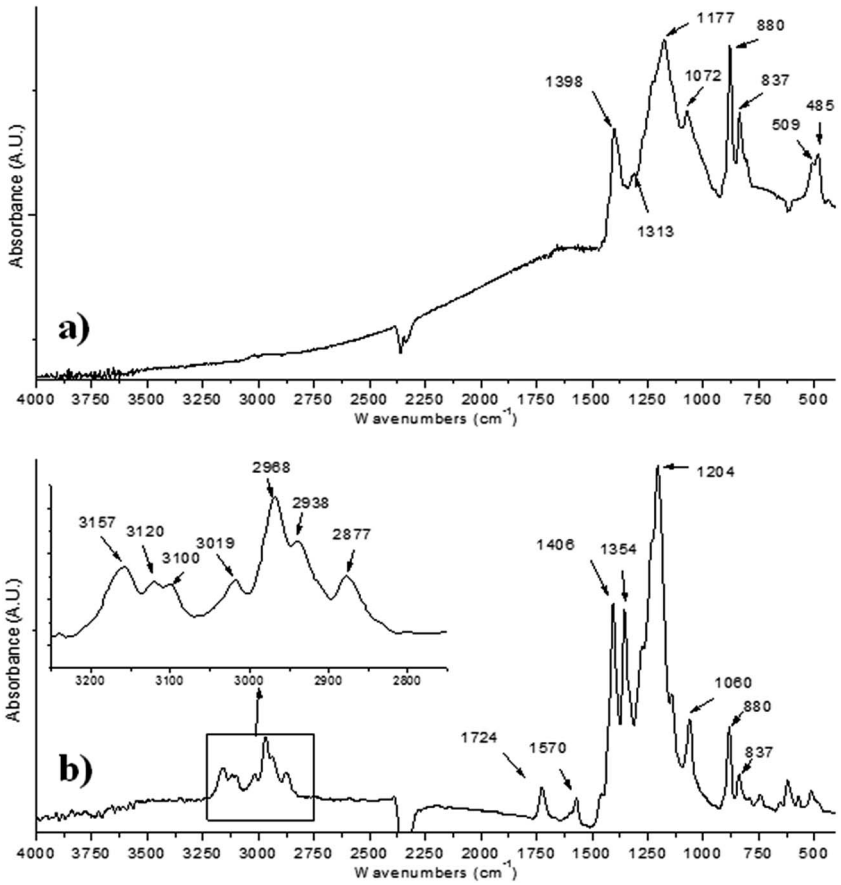

Fig. 2 ATR FTIR spectra (a) PAG (b) PAG–IL.

3.2. Electrical characterization

We studied the switching characteristics of planar structured $AgNO_3$ based RSD with symmetrical Au electrodes. The switching matrix PAG was spin-coated onto the device. The pristine device was found in the high resistance state (HRS) as it can be seen from Fig. 3(a). The RSD had its initial transition from HRS to low resistance state (LRS) at a negative voltage of around −25 V, which corresponds to an electric field of about 25 kV cm^{-1}. Thus, the forming voltage in this particular case is −25 V. The current limit was clamped to 100 μA in both polarities to ensure that the device doesn't get damaged. The initial set process occurring in our experiments can be easily explained by a simple reaction where the Ag^+ ions are being reduced to Ag^0 atoms, which relates to the change in the resistance state of the device from high to low.

$$Ag^+ + e^- \leftrightharpoons Ag$$

The most probable reaction associated with silver reduction is the direct oxidation of oxygen that replaced nitrate in the dissolution of $AgNO_3$ in PVDF-HFP. Thus, the total conduction current can be attributed to the contribution of (1) ionic conduction before switching and (2) non-continuous filamentary conduction after switching.

The application of an initial high electric field is usually common in planar devices where the active distance between the electrodes is relatively high. Once the initial path is set in the polymer matrix, subsequent filament formation is much easier. Cyclic *IV* characterizations at room temperature were performed on the planar devices, as reported in Fig. 3(b). The device exhibits a behavior similar to a random access memory (RAM). The initial voltage sweep was provided in negative polarity and the device was in its HRS. As the voltage reached −25 V, it switched to LRS. This state underwent a transition as soon as the voltage level approached 0 V. Focusing on the positive voltage sweep, the device was again in its HRS, and it moved to LRS at a voltage around 20 V. Thus in the case of planar RSD with PAG, memory was volatile. Fig. 3(c) shows the FESEM image of the characterized RSD with planar structure with PAG as the active switching matrix. It can be seen that silver NPs are homogeneously distributed within the matrix, between the gold electrodes, and that there is no evidence of filament formation between the electrodes after cyclic *I–V* characterization. The ON resistance observed in Fig. 3(b) exceeds 100 kΩ that is much higher than the resistance of a single atomic point (12.9 kΩ),[52] leading to the assumption that the volatile behavior observed is due to a dominant electron tunneling process. A similar reason for volatile behavior has been provided by Krishnan *et al.*[52] Therefore, the switching of the device from HRS to LRS should be due to the formation of a discontinuous metallic filament, where electrons experience hopping between Ag NPs that are not in direct contact,

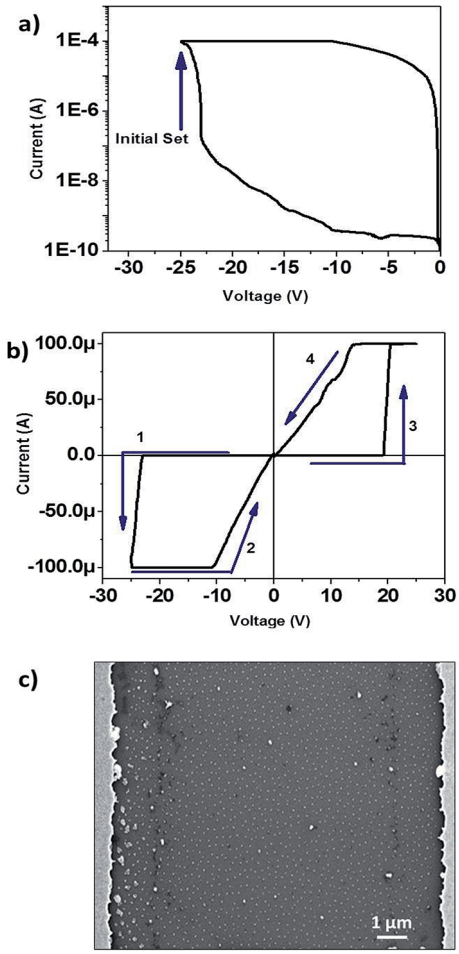

Fig. 3 (a) Initial set process, taking place at −25 V. (b) Cyclic *I–V* measured in the Au/PAG/Au system (c) FESEM image of the device with active switching matrix ($AgNO_3$ and PVDF-HFP) spin coated between the gold electrodes, after electrical characterization.

explaining the relatively high resistance of the device in the LRS. As the voltage approached lower values, the electric field ordering effect was overcome by thermal disorder occurring to the silver NPs.[53] This caused a complete isolation, thus switching the device back to its HRS. Similar results were shown using analogous NCs containing *in situ* generated Ag NPs at a time when hybrid/organic RSDs were not yet known and studied.[54] It was also shown how to control the density and distribution of particles within the polymer matrix by taking advantage of the ion diffusion.[55] However, the working voltage range was quite high in PAG coated RSDs [Fig. 3(b)]. After further studies, it was observed that the addition of 30% IL to the polymer and $AgNO_3$ solution (referred to as PAG–IL) made the electrical response more suitable for low-power electronic devices, leading to a sharp reduction in the forming and set voltage range which is fundamental for a better energy management.

Fig. 4(a) shows the initial cyclic *I–V* curve of the planar RSD using PAG–IL matrix. The device showed a volatile switching behavior. The maximum level of current was set to 100 μA in both polarities. It is interesting to note that the initial switching took place at −2.2 V (forming voltage), which corresponds to a forming field of 2.2 kV cm^{-1} [Fig. 4(b)] and then the switching voltage decreased to lower values, which is usually common in RSDs. This reduction, happening in the initial set voltage range, may be mainly due to the action of IL in the polymer NC. The presence of IL increases the mobility of ions and thus, Ag ions attain a much higher mobility than in the PAG matrix. The effect of IL in the PAG matrix can be studied in a detailed manner by means of DSC and impedance spectroscopy measurements. Fig. 5(a) provides the DSC curves corresponding to PVDF-HFP, PAG and PAG–IL films. It can be seen that the addition of $AgNO_3$ and further addition of IL to PVDF-HFP matrix reduced the depth of the melting peak as well as a shift in the melting peak from 128 °C to 114.5 °C. It's worth mentioning that the melting peak of PAG–IL was broadened when compared to PAG and PVDF-HFP. In other words, there was a plasticizing effect of IL on the polymer matrix. The plasticizing effect reduced dipole–dipole interactions, thus disrupting the transient cross-linkage bonds among the polymer matrix.[56] By integrating the melting peaks of PVDF-HFP, PAG and PAG–IL, it was observed that the area corresponding to the three matrices were 10.5 J g^{-1}, 4.935 J g^{-1} and 1.83 J g^{-1} respectively. This reduction in the area corresponding to PAG–IL indicates that presence of BMI-TFSI facilitates the polymer backbone softening, thus enhancing the segmental motion of the polymer chain thus making it less crystalline. Fig. 5(b) provides the Nyquist plot obtained from the impedance spectra analyzed in the frequency

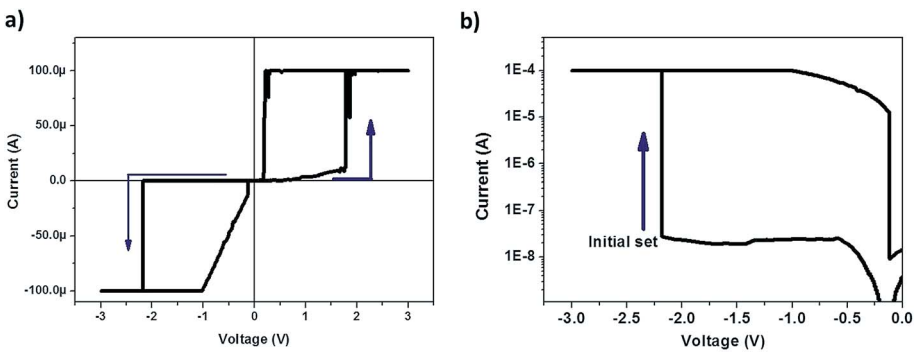

Fig. 4 (a) Initial cyclic *I–V* measured in the Au/PAG–IL/Au system. (b) Zoom on the initial set process taking place at −2.2 V.

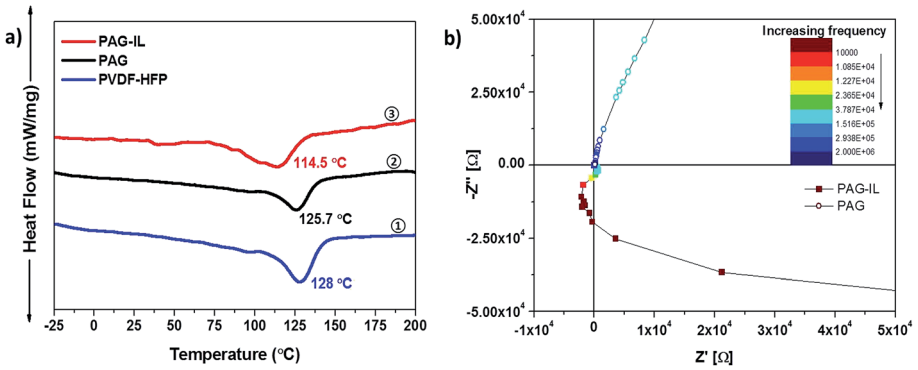

Fig. 5 (a) DSC thermograms of 1 PVDF-HFP 2 PAG and 3 PAG–IL. (b) Nyquist response of the PAG and PAG–IL analyzed from 1 kHz to 10 MHz.

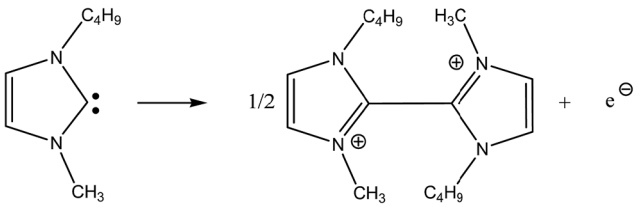

Fig. 6 Electrochemical oxidation of 1-butyl-3-methylimidazol-2-ylidene obtained from BMIM cation.[56]

range [1 kHz, 10 MHz]. The figure provides a limited range of the impedance spectra in order to understand the difference in behavior of PAG and PAG–IL. Data points corresponding to PAG showed an impedance behavior that was dominated by simple diffusion processes. PAG–IL behavior, on the contrary, was much more complex: in the low-frequency regime, we observed a negative differential resistance, taking place from 10 down to 1 kHz, while in the high-frequency regime the behavior recovered the same features of the PAG device. Thus, the data corresponding to PAG–IL was in support of a higher ionic conduction.

In the case with IL, at negative voltages, the silver ion was reduced to silver metal and caused an increase in conduction, as mentioned earlier. On the basis of previous work on electrochemical stability of PAG-based RSDs, the oxidation can be mainly ascribed to the oxidation of 1-butyl-3-methylimidazol-2-ylidene formed by protic dissociation of IL cation [Fig. 6] or the residual DMF.[57,58]

Once the initial forming was observed in the device, the optimal voltage range was investigated, allowing to have a stable and repeatable RS. *I–V* characterization was performed between the voltage range of +0.2 V and −0.2 V. Fig. 7(a) displays the non-volatile switching behavior of the device. The set states were always stable and the threshold voltage corresponding to set was near 0.1 V; while the reset states had slight variations, the reset threshold was in the range of −0.05 V. The different reset compliance, coupled with the optimised voltage bias range and the pre-electrical treatment, changed the memory state of the RSD from volatile to non-volatile [Fig. 7(a)]. After a set of repeated electrical pre-treatment [ESI Fig. S1†] by maintaining 100 μA reset compliance, a non-continuous filament was formed. The stability of the filament can be substantiated by the resistance level observed. The high resistance level (≈2 kΩ) in Fig. 7(b) was lower than the low resistance level (≥10 kΩ) in Fig. 4(b). The formation of a stable filament now enabled the device to set at a much smaller threshold voltage (0.1 V). The reduction in voltage range along with an increase of reset compliance led to the destruction of the formed filament when it reached a negative threshold voltage of −0.05 V. Since the voltage was swept only till −0.2 V, there was no further filament formation, which made the device remain in its HRS until it reached its positive set threshold. Thus, the HRS was maintained until the device reached a positive set threshold where a filament formation took place, which led to a bipolar nonvolatile switching. Thus, it can be stated that a low reset compliance led to a filament in which a spatial gap exists.[59] The increase in conduction in this case can be ascribed to tunneling, and the decrease in conduction can be due to a faster erase process of the thin and unstable filaments leading to a symmetric electrical behavior in the opposite polarity [Fig. 4(a)]. The studies conducted so far on RSDs give more importance to the set compliance, while the reset one is normally less important or not even mentioned.[60] As a matter of fact, compliance-dependent events can be connected to filamentary conduction model. The switching from LRS to HRS can be explained by the breaking of the stable filament (which is not a complete destruction but rather the dissolution of a small portion of it), once the voltage approaches the reset voltage. This breakage happens due to the movement of the silver NPs from the formed filament activated by thermal disordering.

Fig. 7(c) shows the corresponding FESEM image of the device. It was evident that the characterized sample had a non-uniform morphology, where a self-established network was found between the gold electrodes, suggesting the potentiality of our system to realize artificial neuron networks. This irregular peculiar morphology was due to the shrinkage during drying and the partial demixing of the polymer and silver salt. Fig. 7(d) clearly displays the dendritic growth of silver NP filaments (evidenced manually in green to appear from the substrate grey background) between the gold electrodes, three of which are percolating and connecting opposite electrodes

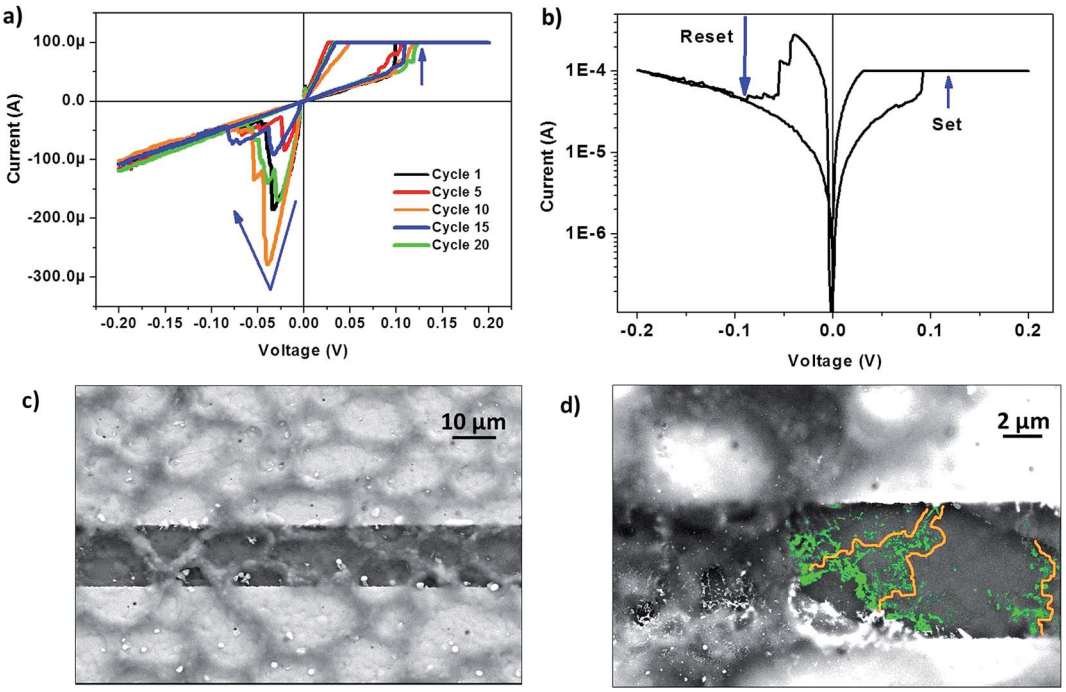

Fig. 7 (a) Cyclic measurement performed at higher reset compliance of 1 mA. (b) Behavior of a single cycle showing bipolar nonvolatile switching behavior at a higher reset compliance. (c) FESEM image of the device with active switching matrix ($AgNO_3$, PVDF-HFP and IL) spin coated between the gold electrodes, after electrical characterization. (d) Magnified portion between the electrodes with percolation paths (evidenced by orange hand drawn lines) and Ag NPs (coloured in green) that bridge the two electrodes.

Table 1 Summary of planar RSD with Au electrodes using PAG and PAG–IL

Switching matrix		Switching behavior	Forming voltage (V)	Set voltage (V)	Reset voltage (V)	I_{on}/I_{off}
PAG		Volatile	−25	20	0.5	Rectifying ratio of 10^4
PAG–IL	100 μA reset current compliance	Volatile	−2.2	1.75	0.2	Rectifying ratio of 2400
	1 mA reset current compliance	Bipolar, non-volatile	−2.2	0.1	−0.05	15 (from retention tests)

(orange lines manually drawn close to those NPs which were seen in contact from highly magnified FESEM images). The formation of dendritic filaments can be related to diffusion-limited aggregation of the silver ions. As it can be seen, there are multiple possible paths between the electrodes. This is similar to the work carried out by Krishnan *et al.*,[28] where a similar planar device was fabricated with symmetric platinum electrodes and Ag–PEO as the polymer composite. Table 1 summarizes the effect of PAG and PAG–IL on the planar resistive switching device with symmetrical Au electrodes. As it can be seen, PAG matrix displayed a nonlinear diode-like behavior. The use of PAG–IL led to the reduction of forming voltage. Furthermore, with the change in the reset compliance level, the device started memorizing its past state. While performing retention tests (see further in the text), it was observed that the I_{on}/I_{off} ratio of PAG–IL coated device with non-volatile state was 700.

Fundamental property of any RSD is its retention. The higher the retention, the better the device. A voltage bias test was carried out on the device in order to check its retention time [Fig. 8]. The test was performed on the planar PAG–IL device at room temperature. The device was read at a voltage of 0.05 V in the set and reset cases. It was seen that the device was

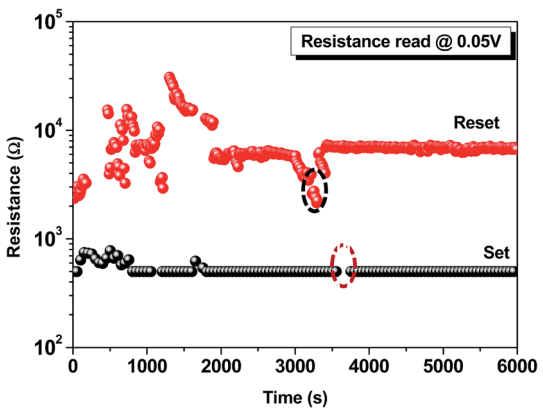

Fig. 8 Retention characteristic of the planar sample with PAG–IL. The sample was read at 0.05 V.

maintained constant set resistance level for more than 6 ks. The set resistance was maintained at 500 Ω. The reset state was fairly unstable for the first 1.5 ks. Later it turned stable and the device maintained this level till 6 ks. The average reset resistance measured by the device during the retention test was about 7 kΩ. The test was interrupted and restarted in order to further confirm non-volatility. It is worth noting that the resistance values before and after the interruption (at 3.6 ks for the set state, red ellipse in Fig. 8 and 3.2 ks for the reset state, black ellipse in Fig. 8) recovered the previous resistance value. This confirmed the non-volatility of the device.

In order to investigate the surface chemistry, especially to understand the oxidation state of Ag on the surface of the device, XPS was conducted on different samples: (1) fresh planar device with deposited PAG–IL, (2) electrically characterized planar device (not aged), (3) one month old characterized planar device (aged) and (4) $AgNO_3$ commercial powder as a reference. Fig. 9 reports the XPS data. From the survey spectra [Fig. 9(a)] we can infer the presence of C, O, N, Ag, F and some impurities due to precursor residues (Si and Cl). To validate what has been previously observed with FT-IR analysis, the N1s peak was checked [Fig. 9(b)], in order to see if nitrogen was still bonded with Ag. The three devices showed signals made up by two bands at ~399 and ~401 eV respectively due to C–NH_2 and C–NH_3, found in IL. No peaks were detected for typical nitrate chemical shift, which should be located at binding energy higher than 403 eV. On the contrary, the $AgNO_3$ commercial powder N1s signal features two separated peaks at 403 and 406.4 eV, which are due to nitrates.[57] Therefore, we can conclude that the Ag nitrate is no longer present inside the polymer matrix (according to FT-IR and XPS techniques sensitivities). Fig. 9(c) shows the Ag3d doublet core-level emission collected from the three devices. For the sake of simplicity, we will comment hereafter only the $Ag3d_{5/2}$ peak deconvolution, while omitting the same information obtained from the $Ag3d_{3/2}$, which is 6.0 eV apart from the previous one. Each peak was deconvoluted by using two components with FWHM values according to what reported in ref. 61–63. As it can be seen in the fresh sample, that has not been electrically characterized, the peak is made up of two bands: the first one at 367.8 eV (40.4%) and the second one at 368.5 eV (59.6%). The first value is typical of Ag_2O,[64] while the second one, which is shifted towards higher binding energies respect to reference value for metallic Ag (368.2 eV), has been assigned to Ag metal NPs;[65] this means that during the deposition the Ag undergo partial reduction, forming metal NPs with a thin layer of silver oxide on the surface. The sample after electrical characterization (not aged) presents the same peak for the Ag_2O (44.2%) chemical shift, while the peak at higher energy is located at 368.2 eV (55.8%), which is the Ag metal foil reference value. So we can state that the measurement changed the state of the Ag filler. The latter graph in Fig. 9(c) is related to the one-month-old tested sample (aged). In this case, the $Ag3d_{5/2}$ peak is composed of two curves which are at 366.5 eV (8.3%) and 367.4 eV (91.7%). The first value is quite unusual for Ag, since it is at very low binding energy. Thomas *et al.*[66] explained this chemical shift with the exposure of the composites to the ambient air, taking origin from Ag_2O. The peak at higher energy, in this case, is due to AgO.[66] So, we can state that the sample which left for one month at ambient conditions (aged) had gone through an ageing process which thickened the oxide layer, since no Ag metal component is present in the peak deconvolution. Moreover, we should keep in mind the surface sensitivity of XPS: for the $Ag3d_{5/2}$ orbital, the attenuation length is such that the signal comes from the top 4 nm of the surface, with most of the signal being from the outermost 1.5 nm.[67] Considering the mean dimension of the Ag NPs (10 to 30 nm), it is clear that XPS gives only information corresponding to the outer surface of particles.

To understand the dependence of device structure on the switching behavior, a stacked structure was realized with PAG–IL switching matrix. As mentioned earlier, the BE was ITO-made

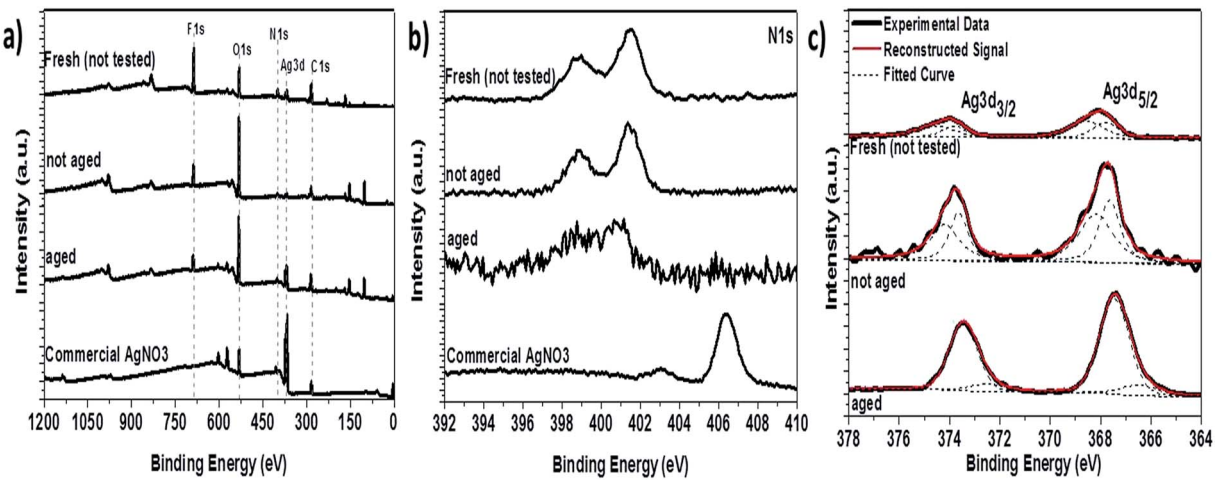

Fig. 9 X-ray photoelectron spectra of NC based RSD prepared with PAG–IL on planar device. (a) Survey spectra. (b) High Resolution (HR) spectra for N1s. (c) HR spectra for Ag3d peaks (black line for experimental data, dashed black line for fitting curves and red line for reconstructed signal). The analyses are made on fresh untested sample (fresh not tested), sample after electrical characterization (not aged), on a one-month-aged sample submitted to electrical characterization (aged), which was kept at ambient conditions, and finally on commercial $AgNO_3$ powder (a and b graphs only).

and the TE was fabricated in gold (4 mm diameter). The device was electrically characterized under ambient temperature, and it was seen that the RSD was exhibiting a bipolar nonvolatile switching behavior. The on resistance and off resistance at a read voltage of −1 V were found to be 50 kΩ and 7 MΩ respectively, thus exhibiting an I_{on}/I_{off} of 150. As in the previous case, in the initial testing conditions, a compliance current level of 1 mA and 100 μA was set in the negative and positive polarities respectively. The active thickness of the PAG–IL matrix was in the range of few hundreds of nm, which was quite thinner than in the planar design. Fig. 10(a) displays the *I–V* plot, and it can be seen that the set process took place in the negative polarity, while the reset took place in the positive polarity. In the earlier case, where PAG–IL was coated onto the planar device with symmetrical gold electrodes, different switching mechanisms were observed according to the electrical parameters set, especially, the compliance current. In the stacked device, different compliance levels were applied for positive and negative polarities, but the system always displayed a nonvolatility. In planar devices featuring symmetrical electrodes, the switching behavior depends on the electrical parameters set, while in stacked devices depends mainly on the electrode's materials and on the active switching matrix thickness. As reported previously, the pristine device was found to be at HRS, and as the voltage reached around −1.7 V, the device took a transition from its high to low resistance state [Fig. 10(b)]. This LRS was continued until the voltage reached +1.6 V at which point the device moved back to its HRS. It was also noted that unlike other cases, where the set potential is reduced after the electroforming, here there was no notable reduction in set voltage. This could be explained by charge confinement within the NPs: initially, the charge gets trapped in the NPs and as the applied field is increased and reaches a certain set threshold (−1.7 kV cm^{-1}), the conductivity of the polymer NC is dramatically increased due to the easy movement of the charge through the polymer matrix which leads to the on state of the device. This state is maintained, until the applied field reaches a critical reset threshold (1.6 kV cm^{-1}), at which point the charges get detrapped thus making the device move back to its initial state.[68] In order to check the stability of the device throughout the working cycles, a pulse test was also performed, where the device was probed at 1 V by setting and resetting at −5 V and 2 V for 500 μs respectively. It was found that the device read almost constant values for about 70 cycles [Fig. 10(c)]. An average set current of about 250 μA and average reset current of about 2 μA was read at 1 V, thus maintaining an I_{on}/I_{off} current ratio of 100. The HRS showed a slight drift in the current with an increase in cycles: this is because the device had a tendency to move to a permanent on state as the cycles proceeded, and thus the current in HRS was slightly increasing. This case, where a stacked structure is considered, is a clear example which explains that device engineering controls the device properties.[69]

It was also observed that the viscosity of PAG–IL was 30 cP, which is an acceptable viscosity for inkjet printing in the case of heated print head, making this switching matrix suitable for flexible printed electronics.

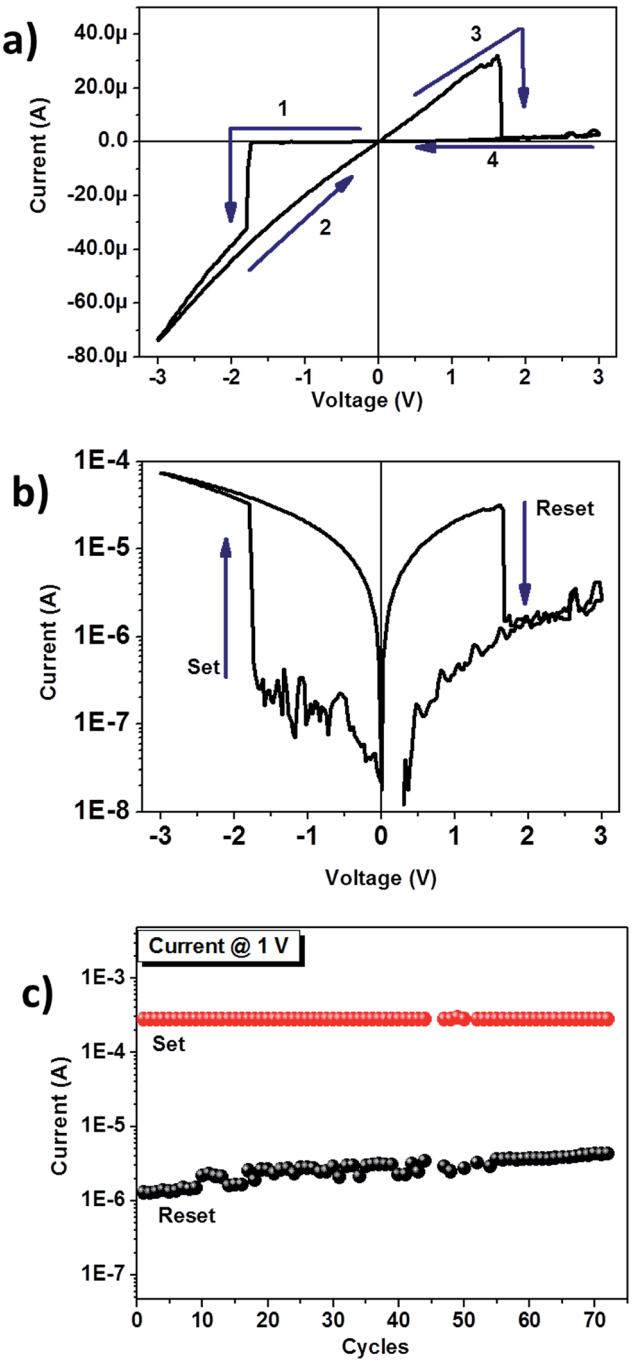

Fig. 10 (a) Cyclic *I–V* measured in the Au/PAG–IL/ITO system. (b) Zoom on the set and reset process in logarithmic scale. (c) Pulse characterization – sample was made to read at 1 V, by setting and resetting the device at −5 V and 2 V for 500 μs.

4. Conclusions

In this work, the resistive switching behavior of Au/$AgNO_3$–PVDF-(with and without) IL/Au based planar structure and Au/$AgNO_3$–PVDF–IL/ITO based stacked structure has been studied. In the initial setup, where the active matrix with no IL was used to build a planar device, the working voltage range was quite high as the effective distance between the electrodes was 10 μm,

and thus, a high electric field was required for the resistive transitions. Moreover, the device exhibited a volatile switching behavior. It was clearly noted that the addition of RTIL to the switching matrix helped in triggering non-volatile memory to the device and also helped in the reduction of the set voltage range, which can be ideally related to improved ionic mobility, facile path for ionic movement and reduced crystallinity and viscosity of the switching matrix. A dendritic filament growth was observed by FESEM imaging in between the electrodes, proving the formation of a silver NP conducting filament which led to the change in the state of the device from HRS to LRS. The compliance current used in the reset condition along with the optimized voltage bias range led to a change in the switching behavior of the device, which can be related to the stability in the formed filament. The electrical behavior was quite stable throughout the working cycles and also showed a retention of more than 6000 seconds with an I_{on}/I_{off} ratio of about 15. The device dependence on the switching matrix (PAG–IL) was also addressed by preparing a stacked structure with asymmetrical electrodes. This configuration revealed a bipolar switching behavior, with an I_{on}/I_{off} ratio of about 10^2. The pulsed characterization showed a stable behavior up to 70 cycles. One of the major advantages guaranteed by the PVDF-HFP matrix is that it can be printed onto flexible substrates, thus widening its scope in the field of printed flexible switching devices. By further tailoring the active switching matrix, the device could be utilized as a building block in future neuromorphic applications.

Acknowledgements

We would like to thank Dr M. Fontana for helping us with FESEM measurements.

References

1 R. Waser and M. Aono, *Nat. Mater.*, 2007, **6**, 833–840.
2 D. H. Kwon, K. M. Kim, J. H. Jang, M. J. Jeon, M. H. Lee, G. H. Kim, X. S. Li, G. S. Park, B. Lee, S. Han, M. Kim and C. S. Hwang, *Nat. Nanotechnol.*, 2010, **5**, 148–153.
3 C. G. Ronald Naber, K. Asadi, W. M. Paul Blom, D. M. de Leeuw and B. de Boer, *Adv. Mater.*, 2010, **22**, 933–945.
4 L. P. Ma, J. Liu and Y. Yang, *Appl. Phys. Lett.*, 2002, **80**, 2997–2999.
5 L. O. Chua, *IEEE Trans. Circuit Theory*, 1971, **18**, 507–519.
6 D. B. Strukov, G. S. Snider, D. R. Stewart and R. S. Williams, *Nature*, 2008, **453**, 80–83.
7 J. Sullaphen, K. Bogle, X. Cheng, J. M. Gregg and N. Valanoor, *Appl. Phys. Lett.*, 2012, **100**, 203115.
8 G. M. Janousch, I. Meijer, U. Staub, B. Delley, S. F. Carg and B. P. Andreasson, *Adv. Mater.*, 2007, **19**, 2232–2235.
9 M. Li, F. Zhuge, X. Zhu, K. Yin, J. Wang, Y. Liu, C. He, B. Chen and R. W. Li, *Nanotechnology*, 2010, **21**, 425202.
10 V. Sascha and M. Xiangkang, *Sci. Rep.*, 2015, **5**, 11657.
11 H. Sun, Q. Liu, C. Li, S. Long, H. Lv, C. Bi, Z. Huo, L. Li and M. Liu, *Adv. Funct. Mater.*, 2014, **24**, 5679–5686.
12 J. G. Simmons and R. R. Verderber, *Proc. R. Soc. A*, 1967, **301**, 77–102.
13 N. R. Tu and K. C. Kao, *J. Appl. Phys.*, 1999, **85**, 7267.
14 R. A. Nawrocki, R. M. Voyles and S. E. Shaheen, *Polymer and Nanoparticle–Composite Bistable Devices: Physics of Operation and Initial Applications*, ed. R. Kozma, R. E. Pino and G. E. Pazienza, Springer, Netherlands, 2012, pp. 291–314.
15 G. Casula, P. Cosseddu, Y. Busby, J. J. Pireaux, M. Rosowski, B. T. Szczesna, K. Soliwoda, G. Celichowski, J. Grobelny, J. Novak, R. Banerjee, F. Schreiber and A. Bonfiglio, *Org. Electron.*, 2015, **18**, 17–23.
16 Y. Chen, B. Zhang, G. Liu, X. Zhuang and E. T. Kanq, *Chem. Soc. Rev.*, 2012, **41**, 4688–4707.
17 W. P. Lin, S. J. Liu, T. Gong, Q. Zhao and W. Huang, *Adv. Mater.*, 2014, **26**, 570–606.
18 A. Sawa, *Mater. Today*, 2008, **11**, 1128–1136.
19 D. H. Kwon, K. M. Kim, J. H. Jang, J. M. Jeon, M. H. Lee, G. H. Kim, X. S. Li, G. S. Park, B. Lee, S. Han, M. Kim and C. S. Hwang, *Nat. Nanotechnol.*, 2010, **5**, 148–153.
20 Y. C. Yang, F. Pan, Q. Liu, M. Liu and F. Zeng, Fully room-temperature-fabricated nonvolatile resistive memory for ultrafast and high-density memory application, *Nano Lett.*, 2009, **9**, 1636–1643.
21 T. Sakamoto, K. Lister, N. Banno, T. Hasegawa, K. Terabe and M. Aono, *Appl. Phys. Lett.*, 2007, **91**, 092110.
22 G. S. Park, X. S. Li, D. C. Kim, R. J. Jung, M. J. Lee and S. Seo, *Appl. Phys. Lett.*, 2007, **91**, 222103.
23 Z. Xu, Y. Bando, Y. Wang, X. Bai and D. Golberg, *ACS Nano*, 2010, **4**, 2515–2522.
24 T. Fujii, M. Arita, Y. Takahashi and I. Fujiwara, *Appl. Phys. Lett.*, 2011, **98**, 212104.
25 R. Waser, R. Dittmann, G. Staikov and K. Szot, *Adv. Mater.*, 2009, **21**, 2632–2663.
26 I. Valov, R. Waser, J. R. Jameson and M. N. Kozicki, *Nanotechnology*, 2011, **22**, 289502.
27 W. P. Lin, S. J. Liu, T. Gong, Q. Zhao and W. Huang, *Adv. Mater.*, 2014, **26**, 570–606.
28 K. Krishnan, T. Tsuruoka, C. Mannequin and M. Aono, *Adv. Mater.*, 2016, **28**, 640–648.
29 M. Naushada, Z. A. Alothmana, A. B. Khanb and M. Ali, *Int. J. Biol. Macromol.*, 2012, **51**, 555–560.
30 J. W. Park, K. Yamauchi, E. Takashima, N. Tachikawa, K. Ueno, K. Dokko and M. Watanabe, *J. Phys. Chem. C*, 2013, **117**, 4431–4440.
31 M. Dobbelin, R. Marcilla, M. Salsamendi, C. Pozo Gonzalo, P. M. Carrasco, J. A. Pomposo and D. Mecerreyes, *Chem. Mater.*, 2007, **19**, 2147–2149.
32 T. M. W. J. Bandara and B. E. Mellander, *Evaluation of Mobility, Diffusion Coefficient and Density of Charge Carriers in Ionic Liquids and Novel Electrolytes Based on a New Model for Dielectric Response*, ed. A. Kokorin, InTech, 2011, DOI: 10.5772/15183.
33 T. Subburaj, Y. N. Jo and C. W. Lee, *Curr. Appl. Phys.*, 2014, **14**, 1022–1027.
34 F. Wu, T. Feng, Y. Bai and C. Wu, *Solid State Ionics*, 2009, **180**, 677–680.
35 N. Ataollahi, A. Ahmad, H. Hamzah, M. Y. A. Rahman and N. S. Mohamed, *Int. J. Electrochem. Sci.*, 2012, **7**, 6693–6703.

36 A. Fernicola, B. Scrosati and H. Ohno, *Ionics*, 2006, **12**, 95–102.
37 M. Stoppa and A. Chiolerio, *Sensors*, 2014, **14**, 11957–11992.
38 Y. H. Hwan, J. S. Seo, J. M. Yun, H. Park, S. Yang, S. H. Ko Park and B. S. Bae, *NPG Asia Mater.*, 2013, **5**, e45.
39 B. Mukherjee and M. Mukherjee, *Appl. Phys. Lett.*, 2009, **94**, 173510.
40 B. Pradhan, K. Sudip, K. Batabyal and A. J. Pal, *Appl. Phys. Lett.*, 2006, **88**, 093106.
41 D. Liu, H. Cheng, X. Zhu, G. Wang and N. Wang, *ACS Appl. Mater. Interfaces*, 2013, **5**, 11258–11264.
42 R. J. Tseng, J. Huang, J. Ouyang, R. B. Kaner and Yang, *Nano Lett.*, 2005, **5**, 1077–1080.
43 S. Ramesh and O. P. Ling, *Polym. Chem.*, 2010, **1**, 702–707.
44 G. I. N. Waterhouse, A. G. Bowmaker and J. B. Metson, *Phys. Chem. Chem. Phys.*, 2001, **3**, 3838–3845.
45 I. Rey, P. Johansson, J. Lindgren, J. C. Lassegues, J. Grondin and L. Servant, *J. Phys. Chem. A*, 1998, **102**, 3249–3258.
46 Y. Jeon, J. Sung, D. Kim, C. Seo, H. Cheong, Y. Ouchi, R. Ozawa and H. Hamaguchi, *J. Phys. Chem. B*, 2008, **112**, 923–928.
47 J. B. Brubach, A. Mermet, A. Filabozzi, A. Gerscel, D. Lairez, M. P. Krafft and P. Roy, *J. Phys. Chem. B*, 2001, **105**, 430–435.
48 M. Donato, S. Bocchini, G. Canavese and M. Lombardi, *Key Eng. Mater.*, 2014, **605**, 263–266.
49 E. R. Talaty, S. Raja, V. J. Storhaung, A. Dolle and W. R. Carper, *J. Phys. Chem. B*, 2004, **108**, 13177–13184.
50 D. A. Carter, J. E. Pemberton and K. J. Woelfel, *J. Phys. Chem. B*, 1998, **102**, 9870–9880.
51 J. Grondin, J. C. Lassegues, D. Cavagnat, T. Buffeteau, P. Johansson and R. Holomb, *J. Raman Spectrosc.*, 2011, **42**, 733–743.
52 K. Krishnan, M. Aono and T. Tsuruoka, *Nanoscale*, 2016, **8**(29), 13976–13984.
53 R. Mutiso, J. Kikkawa and K. Winey, *Appl. Phys. Lett.*, 2013, **103**, 223302.
54 A. Chiolerio and M. Sangermano, *Mater. Sci. Eng., B*, 2012, **177**, 373–380.
55 A. Chiolerio, I. Roppolo and M. Sangermano, *RSC Adv.*, 2013, **3**, 3446–3452.
56 S. Ramesh, C. E. Liew and K. Ramesh, *J. Non-Cryst. Solids*, 2011, **357**, 2132–2138.
57 I. Chiarotto, M. Feroci, G. Forte and A. Inesi, *Electrochim. Acta*, 2015, **176**, 627–635.
58 H. Lund, Practical problems in Electrolysis, *Organic electrochemistry*, ed. O. Hammerich and H. Lund, Marcel Dekker Inc., New York, 2000, p. 223.
59 D. Liu, N. Wang, G. Wang, Z. Shao, X. Zhu, C. Zhang and H. Cheng, *Appl. Phys. Lett.*, 2013, **102**, 134105.
60 Y. Li, P. Yuan, L. Fu, R. Li, X. Gao and C. Tao, *Nanotechnology*, 2015, **26**, 391001.
61 G. B. Hoflund, Z. F. Hazos and G. N. Salaita, *Phys. Rev. B: Condens. Matter Mater. Phys.*, 2000, **62**, 11126–11133.
62 J. F. Weaver and G. B. Hoflund, *J. Phys. Chem.*, 1994, **98**, 8519–8524.
63 V. K. Kaushik, *J. Electron Spectrosc. Relat. Phenom.*, 1991, **56**, 273–277.
64 Y. Busby and J. J. Pireaux, *J. Electron Spectrosc. Relat. Phenom.*, 2014, **192**, 13–18.
65 H. S. Shin, H. C. Choi, Y. Jung, S. B. Kim, H. J. Song and H. J. Shin, *Chem. Phys. Lett.*, 2004, **383**, 418–422.
66 S. Thomas, S. K. Nair, E. M. Jamal, S. H. Al Harthi, M. R. Varma and M. R. Anantharaman, *Nanotechnology*, 2008, **19**, 075710.
67 G. I. N. Waterhouse, G. A. Bowmaker and J. B. Metson, *Appl. Surf. Sci.*, 2001, **183**, 191–204.
68 Y. Wang, X. Yan and R. Dong, *Org. Electron.*, 2014, **15**, 3476–3481.
69 G. Dearnaley, A. M. Stoneham and D. V. Morgan, *Rep. Prog. Phys.*, 1970, **33**, 1129–1191.